drones

MDPI

Article

A New Autonomous Method of Drone Path Planning Based on Multiple Strategies for Avoiding Obstacles with High Speed and High Density

Tongyao Yang [1], Fengbao Yang [1,*] and Dingzhu Li [1,2]

[1] School of Information and Communication Engineering, North University of China, Taiyuan 030051, China; b20210509@st.nuc.edu.cn (T.Y.); dnacti@163.com (D.L.)
[2] North Automatic Control Technology Institute, Taiyuan 030051, China
* Correspondence: yangfb@nuc.edu.cn

Abstract: Path planning is one of the most essential parts of autonomous navigation. Most existing works are based on the strategy of adjusting angles for planning. However, drones are susceptible to collisions in environments with densely distributed and high-speed obstacles, which poses a serious threat to flight safety. To handle this challenge, we propose a new method based on Multiple Strategies for Avoiding Obstacles with High Speed and High Density (MSAO2H). Firstly, we propose to extend the obstacle avoidance decisions of drones into angle adjustment, speed adjustment, and obstacle clearance. Hybrid action space is adopted to model each decision. Secondly, the state space of the obstacle environment is constructed to provide effective features for learning decision parameters. The instant reward and the ultimate reward are designed to balance the learning efficiency of decision parameters and the ability to explore optimal solutions. Finally, we innovatively introduced the interferometric fluid dynamics system into the parameterized deep Q-network to guide the learning of angle parameters. Compared with other algorithms, the proposed model has high success rates and generates high-quality planned paths. It can meet the requirements for autonomously planning high-quality paths in densely dynamic obstacle environments.

Keywords: hybrid action space; path planning; obstacle avoidance decision-making; interfered fluid dynamical system; deep reinforcement learning

Citation: Yang, T.; Yang, F.; Li, D. A New Autonomous Method of Drone Path Planning Based on Multiple Strategies for Avoiding Obstacles with High Speed and High Density. *Drones* **2024**, *8*, 205. https://doi.org/10.3390/drones8050205

Academic Editor: Chao Huang

Received: 21 March 2024
Revised: 3 May 2024
Accepted: 14 May 2024
Published: 16 May 2024

1. Introduction

As a critical technology reflecting the autonomous control capability of drones, the essence of path planning is to design a collision-free optimal path in the three-dimensional space environment from the starting position to the destination [1]. With the continuous development of air combat information technology, the airspace environment of drones is becoming increasingly complex. This complexity is reflected in the dense distribution of and dynamic changes in obstacles. The complex airspace environment presents significant challenges to the safety of drone flights. It is crucial to achieve autonomous obstacle-avoidance decision-making for drones to enhance the intelligent decision-making capabilities of control systems.

At present, in the field of path planning research, scholars from various countries are concentrating on improving the efficiency, completeness, and optimality of search paths. The achievements made are mainly divided into graph search algorithms [2–7], fluid/potential field algorithms [8–14], heuristic algorithms [15–19], and artificial intelligence learning algorithms. Graph search is the most effective search method for finding the shortest path in the static road network. Reference [5] used the Dijkstra algorithm to implement real-time path planning by defining the interest points of obstacles. However, path planning cannot be efficiently performed for dynamic obstacles. Fluid/potential field algorithms can generate a smooth virtual field based on the position of a target and the

distribution of obstacles. The algorithms offer clear advantages in the smooth control of path planning and are widely utilized. Reference [11] introduced virtual sub-targets into an artificial potential field to achieve reasonable obstacle avoidance in complex environments. However, the algorithm lacks global information, making it only suitable for obstacle avoidance in local space. Reference [17] proposed a sand cat algorithm with learning behavior, which enables the UAV to plan a safe and feasible path at low cost. However, heuristic algorithms are typically suitable for simple or small environments. Their search efficiency decreases when the planning environment is complex, making it easy to become trapped in local optimal solutions. Observing that the path planning problem is a sequential decision-making problem, researchers turn to reinforcement learning (RL)-based methods [20–22]. Reference [22] built a maneuvering decision model using Q-learning and realized independent path planning in simulation environments. By integrating deep learning technology with reinforcement learning, deep reinforcement learning (DRL) [23–31] can acquire knowledge from the interaction between agents and the environment using neural networks. This approach is more closely aligned with the essence of biologic learning and can cope with complex and dynamic airspace environments. In addition, based on the nonlinear learning ability of neural networks, DRL can effectively extract useful features from high-dimensional data, such as continuous historical trajectory information of obstacles and the attributes of obstacles affecting the effectiveness of path planning. Reference [26] achieved autonomous navigation of drones in a multi-obstacle environment based on the twin delayed deep deterministic policy gradient (TD3) network. Reference [27] proposed the construction of sparse rewards to achieve automatic obstacle avoidance for drones based on the asynchronous advantage actor–critic (A3C) network. Reference [28] utilized the Q function of enhanced dueling double deep Q-networks (D3QN) with priority to implement UAV path planning in dynamic scenarios.

However, in the above research, the path planning environment is relatively simple. When the airspace environment of the drone is extremely complex, such as conducting reconnaissance, interpenetration, and other tasks in air combat, the obstacles may include vehicle-mounted phased array radar, anti-aircraft guns, electronic warfare aircraft, and other aircraft with striking capability. These obstacles are characterized by a highly dense distribution and high-speed dynamics. In such complex dynamic environments, it is challenging to plan safe routes effectively by relying solely on the decision of angle adjustment to avoid obstacles. Therefore, this paper aims to enhance the obstacle-avoidance decision-making of drones in complex airspace environments. This is achieved by adjusting the flight speed or direction or removing obstacles that significantly impact the quality of path planning in order to improve autonomous route planning capabilities.

Compared to discrete action spaces or continuous action spaces, hybrid action spaces can better describe complex problems by combining decision variables from multiple dimensions. This flexibility makes hybrid action spaces have more practical significance. In response to the diverse obstacle-avoidance decisions and their unique descriptive parameters, the hybrid action space can more effectively describe this situation, providing a research foundation. In addition, some scholars have developed deep reinforcement learning networks for hybrid action learning [32,33], which have been widely used in various decision-making problems such as games [34,35] and resource management [36,37].

Therefore, taking deep reinforcement learning as the core technical approach and analyzing the motion rules of drones, this paper proposes the Multiple Strategies for Avoiding Obstacles with High Speed and High Density (MSAO2H) model inspired by hybrid action space. The model aims to meet the requirements of autonomy and high quality in path planning for drones. The main contributions of this paper are:

(1) We propose three types of obstacle-avoidance decisions for drones. This is the first study on obstacle avoidance using three decisions: adjusting angles, adjusting speed, and obstacle clearance. Based on the hybrid action space, discrete obstacle-avoidance decisions and continuous action parameters are combined to improve the efficiency of path planning.

(2) In order to improve the learning efficiency of angle parameters, the interfered fluid dynamical system (IFDS) is innovatively introduced in the training process of the parametric deep Q network (PDQN). The model combines the advantages of PDQN in autonomous learning and IFDS in generating high-quality paths in complex dynamic obstacle environments, thereby enhancing the quality of path planning.

(3) Random environments with densely distributed and high-speed obstacles are designed in the GYM platform. The neural network is used to explore the interaction law between the drone and obstacle environments. The validity of the proposed method is verified in the scenarios.

The remainder of this paper is organized as follows. Section 2 briefly introduces the problem of path planning for drones. Section 3 introduces the relevant theories. Section 4 introduces the proposed method. Section 5 shows the simulation experiments and discussion. Section 6 presents the conclusions of this study.

2. Description of the Obstacle Environments

The complexity of the airspace environment is mainly reflected in the dense distribution of and dynamic changes in obstacles. Therefore, the obstacles in airspace are equivalent to moving spheres with a large radius in this paper, as shown in Equation (1) [38]:

$$\Gamma(\xi) = \left(\frac{x - x_0}{R_{obs}}\right)^2 + \left(\frac{y - y_0}{R_{obs}}\right)^2 + \left(\frac{z - z_0}{R_{obs}}\right)^2 \quad (1)$$

where $\xi = (x, y, z)$ represents the position of the drone, (x_0, y_0, z_0) represents the center point coordinates of the obstacle, and $R_{obs} \in [2500, 8500]$ m represents the radius of the obstacle.

In addition, we simulated the trajectories of obstacles through four different motion modes: static obstacles (Model 0), uniform linear motion (Model 1), horizontal uniform circular motion (Model 2), and serpentine motion (Model 3), whose motion laws are illustrated in Figure 1.

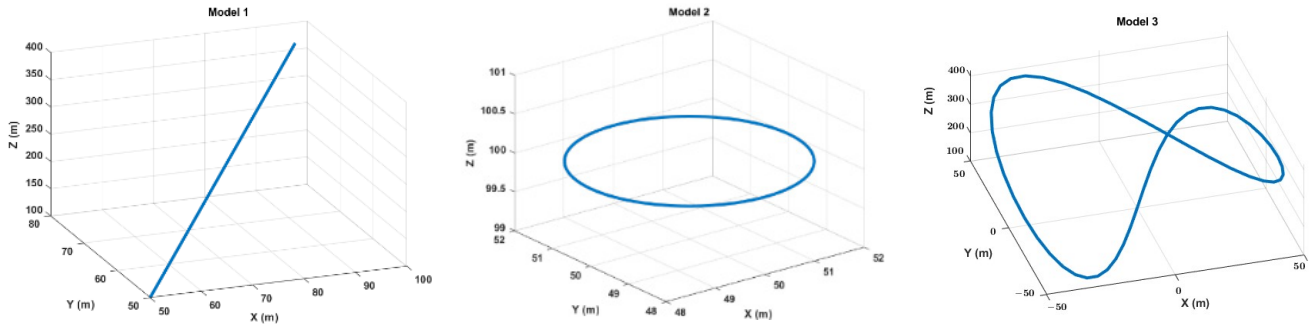

(**a**) (**b**) (**c**)

Figure 1. Obstacle-avoidance decision space. (**a**) Model 1; (**b**) Model 2; (**c**) Model 3.

Based on the characteristics of obstacles, the blue dot in Figure 2 represents the starting point of the drone, which is fixed at [0, 0, 10,000]. The magenta dot represents the goal point of the drone, which is fixed at [10,000, 10,000, 20,000]. The initial positions of multiple obstacles are randomly simulated in the airspace range of $100 \times 100 \times 30$ km^3. The number of obstacles N is $[8, 25]$. We introduced noise to simulate the motion uncertainty of obstacles, making the simulated obstacles closer to those in the real world.

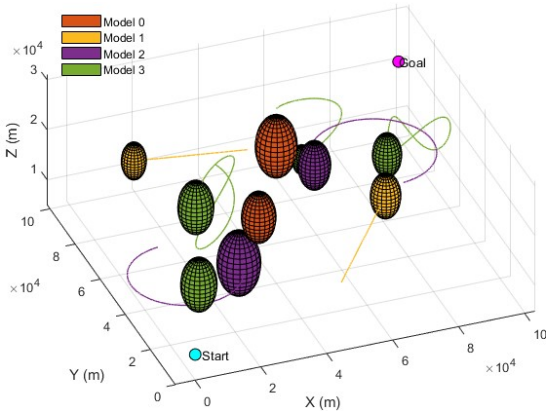

Figure 2. Schematic diagram of dynamic obstacle environment.

In addition, the quality of path planning needs to be evaluated from the aspects of path length P_p, tortuosity C_p, and relative distance to the nearest obstacle D_p. When P_p is smaller, C_p is smaller, and D_p is farther, the comprehensive quality of the planned path is better, enabling it to better fulfill the high-quality planning requirements for paths in complex obstacle environments. The corresponding calculation formulas are as follows:

$$P_p = \sum_{n=1}^{N-1} \sqrt{(p_{n+1}(x) - p_n(x))^2 + (p_{n+1}(y) - p_n(y))^2 + (p_{n+1}(z) - p_n(z))^2} \tag{2}$$

$$C_p = \sum_{n=1}^{N-2} \operatorname{acos}(\overrightarrow{P_nP_{n+1}} \times \overrightarrow{P_{n+1}P_{n+2}}) / (\left|\overrightarrow{P_nP_{n+1}}\right| \times \left|\overrightarrow{P_{n+1}P_{n+2}}\right|) \tag{3}$$

$$D_p = \min(\left|\sqrt{(P_n(x) - O_i(x))^2 + (P_n(y) - O_i(y))^2 + (P_n(z) - O_i(z))^2}\right| - R_{obs}(i)) \tag{4}$$

where O_i is the position of the i-th obstacle, $R_{obs}(i)$ is the corresponding influence radius, and $p_n = (p_n(x), p_n(y), p_n(z))$ is the position of the n-th route node.

This research focuses on how one can autonomously plan high-quality paths in response to the large number of obstacles in the airspace and the dynamic changes in their positions.

3. Related Theories

3.1. PDQN

The PDQN is a kind of value-based reinforcement learning [39], which provides a general framework for effectively solving hybrid action space problems. As shown in Figure 3, the hybrid action space is represented as a tuple (k, x), where discrete actions are selected from a finite set $\mathcal{A}_d = \{k_1, k_2, \ldots, k_k\}$ and each action $k \in \mathcal{A}_d$ has a set of real-valued continuous parameters $x_a \subseteq \mathbb{R}^{m_a}$ [40].

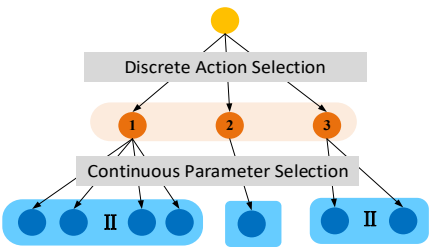

Figure 3. Schematic diagram of hybrid action space structure.

The Bellman equation of the PDQN can be written as Equation (5):

$$Q(s_t, k_t, x_t) = E_{r_t, s_{t+1}}[r_t + \gamma \text{maxsup} Q(s_{t+1}, k_t, x_t) | s_t = s, a_t = (k_t, x_t)] \tag{5}$$

where s, r, a represent state space, rewards, and action respectively, and γ represents discount factor. Here, inside the conditional expectation on the right-hand side of Equation (5), they first solve Equation (6) for each $k \in [K]$:

$$x_k^* = \text{argsup} x_{k \in \chi_k} Q(s_{t+1}, k, x_k) \tag{6}$$

Then, we select the largest $Q(s_{t+1}, k, x_k^*)$. When the function Q is fixed, Equation (6) can be seen as the function $x_k^Q : S \to \chi_k$. Then, the Bellman equation can be written as:

$$Q(s_t, k_t, x_t) = E_{r_t, s_{t+1}}[r_t + \gamma \text{max} Q(s_{t+1}, k_t, x_k^Q(s_{t+1})) | s_t = s] \tag{7}$$

The value network $Q(s, k, x_k, w)$ is used to approximate $Q(s_t, k_t, x_t)$, and the strategy network $x_k^Q(s, \theta)$ is used to approximate x_k^Q. w, θ are the parameters of the value network and the policy network, respectively. The loss functions are as shown in Equation (8), where y_t is the loss function.

$$\ell_t^Q(w) = \frac{1}{2}[Q(s_t, k_t, x_{k_t}; w) - y_t]^2, \ell_t^\Theta(\theta) = -\sum_{k=1}^{K} Q(s_t, k, x_k(s_t; \theta); w_t) \tag{8}$$

Based on the nonlinear mapping ability of PDQN, it can extract more meaningful features from the original input, helping the agent learn the hybrid action parameters better.

3.2. IFDS

The path planning method based on the IFDS simulates the macroscopic characteristics of water flow [41]. This method makes the generated path have the advantage of being smoother.

(1) Build the initial flow field model. Since the initial flow field model is not set to be affected by obstacles, the expression of the initial fluid vector velocity is as follows:

$$\mu = -V\left[\frac{x - x_d}{d}, \frac{y - y_d}{d}, \frac{z - z_d}{d}\right] \tag{9}$$

where $d = \sqrt{(x - x_d)^2 + (y - y_d)^2 + (z - z_d)^2}$ represents the Euclidean distance between the point (x, y, z) and the target point.

(2) Build the disturbed flow field model. The obstacles can cause disturbance to the initial flow field, and the impact expression is as follows:

$$M(p) = I - \frac{n(p)(n(p))^T}{|\Gamma(p)|^{\frac{1}{\rho}}(n(p))^T n(p)} + \frac{t(p)(n(p))^T}{|\Gamma(p)|^{\frac{1}{\sigma}}\|t(p)\|\|n(p)\|} \tag{10}$$

I is the unit attraction matrix, and the second and third terms are the repulsion matrix and the tangential matrix, respectively. $t(p) = R^I(p)[\cos\theta, \sin\theta, 0]^T$ is the tangential matrix. $n(p)$ is a radial normal vector: $n(p) = \left[\frac{\partial \Gamma p}{\partial x}, \frac{\partial \Gamma p}{\partial y}, \frac{\partial \Gamma p}{\partial z}\right]^T$.

(3) Calculate the confluent flow field $\overline{u}(P) = M(P)u(P)$ and obtain the next point $P^* = P + \overline{u}(P)\Delta t$. In this way, a series of scattered points are obtained through iterative solutions and connected to form an interfered streamline, that is, the planned path.

θ, ρ, σ determine the shape and direction of the planned path. The larger ρ or σ is, the more drastically and earlier the agent avoids the obstacles.

4. Method

The MSAO2H model mainly consists of four components: the obstacle avoidance strategy space, the state space of obstacle environments, the reward of obstacle avoidance actions, and the training of the PDQN-IFDS.

4.1. Construction of the Multiple Obstacle-Avoidance Decision Space for Drones

According to the characteristics of obstacle environments and the needs of path planning described in Section 2, the obstacle-avoidance actions of drones include adjusting angles, adjusting speed, and obstacle clearance in this paper.

As shown in Figure 4a, the obstacle can be avoided by accelerating without changing the flight angles. In Figure 4b, the obstacle *R1* has a larger influence range. After removing *R1*, the obstacle environment is greatly simplified. Therefore, the quality of path planning can be improved by adjusting the speed of drones or clearing obstacles to avoid dynamic obstacles. The specific analysis is as follows:

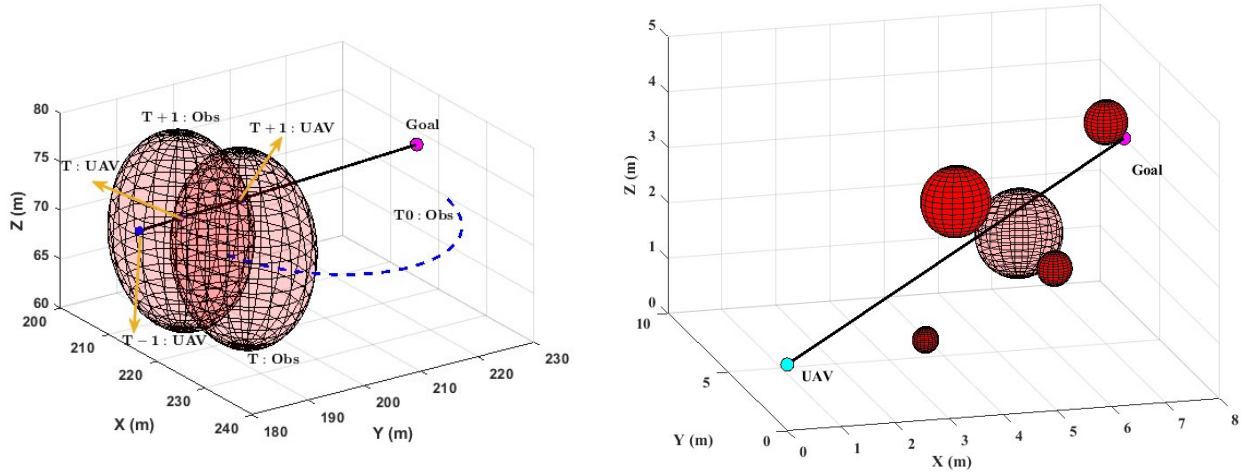

(**a**) (**b**)

Figure 4. Obstacle-avoidance decision space: (**a**) adjusting speed and (**b**) clearing obstacle R1.

(1) Adjusting angles: Considering the angular rate constraints of the climb angle and heading angle, the climb angle and heading angle at the next moment are adjusted as $\chi_{\alpha f}$ and $\gamma_{\alpha f}$, respectively:

$$\chi_{\alpha f} = \begin{cases} \chi_c, & |\dot{\chi}_c| \le \dot{\chi}_{\max} \\ \chi_c + \dot{\chi}_{\max}\Delta T, & \dot{\chi}_c > \dot{\chi}_{\max} \\ \chi_c - \dot{\chi}_{\max}\Delta T, & \dot{\chi}_c < -\dot{\chi}_{\max} \end{cases}, \gamma_{\alpha f} = \begin{cases} \gamma_c, & |\dot{\gamma}_c| \le \dot{\gamma}_{\max} \\ \gamma_c + \dot{\gamma}_{\max}\Delta T, & \dot{\gamma}_c > \dot{\gamma}_{\max} \\ \gamma_c - \dot{\gamma}_{\max}\Delta T, & \dot{\gamma}_c < -\dot{\gamma}_{\max} \end{cases} \tag{11}$$

where $\dot{\chi}_c = \left(\chi_c - \chi_{af}(t)\right)/\Delta T$, $\dot{\gamma}_c = \left(\gamma_c - \gamma_{af}(t)\right)/\Delta T$ are the change rates of the climb angle and heading angle at the next moment, and $\dot{\chi}_{\max}$ and $\dot{\gamma}_{\max}$ are the maximum angular rates of the climb angle and heading angle.

(2) Adjusting speed: When the parameter α of the adjusting speed is obtained, the flight speed of the drone at the next moment is $V = V(t) + a\Delta T, a \in (-a_{\max}, a_{\max})$. Considering the speed limit of drones, the speed is corrected according to Equation (12):

$$V = \begin{cases} V_{\max}, & V > V_{\max} \\ V, & V_{\min} \le V \le V_{\max} \\ V_{\min}, & V \le V_{\min} \end{cases} \tag{12}$$

(3) Clearing obstacles: When remove = 0, this indicates that the clearing operation is not performed, and the drone interacts with the obstacle environment according to

the original motion law. When remove = 1, the drone clears the obstacle, the number of obstacles decreases, and the maximum residual cost of the drone changes to $q = q(t) - r_{\cos}$. At the next moment, the drone obtains a new state space by interacting with the remaining obstacles. The initial remaining cost of obstacle clearance for the drone is 0.9.

Based on the above steps, the formula for calculating the position of the drone at the next moment is as follows:

$$\begin{bmatrix} x(t+1) \\ y(t+1) \\ z(t+1) \end{bmatrix} = \begin{bmatrix} x(t) \\ y(t) \\ z(t) \end{bmatrix} + \begin{bmatrix} V(t)\cos\gamma_{af}(t)\cos\chi_{af}(t) \\ V(t)\cos\gamma_{af}(t)\sin\chi_{af}(t) \\ V(t)\sin\gamma_{af}(t) \end{bmatrix} \Delta T \tag{13}$$

4.2. Construction of the State Space

In order to improve the learning efficiency of the clearing parameter in specific situations, the descriptive factors r_{cro}, r_{atts}, and r_{attv} of obstacle attributes are constructed. The indicators are described as follows:

r_{cro} represents the cost of the drone to clear the obstacle, which is mainly determined by the vulnerability of obstacles. The greater the vulnerability of obstacles, the more difficult they are for the drone to clear, resulting in higher costs. In this paper, r_{cro} is set as [0.1,0.9].

r_{atts} represents the success rate of obstacle clearance, which is mainly affected by the speed v_o of obstacles and the speed v_d of the drone. When the obstacle is static, the success rate of clearance is the highest. When the speed of a dynamic obstacle is greater, the success rate of clearance is lower. Therefore, the calculation formula of r_{atts} is shown in Equation (14):

$$r_{atts} = \exp(-\frac{v_o}{v_d}) \tag{14}$$

r_{attv} represents the benefits brought by removing obstacles for path planning, and the calculation is shown in Equation (15). The former term represents the obstruction degree of the obstacle, and the latter term represents the dispersion of the obstacle. w_1, w_2 are the corresponding weights.

$$r_{attv} = w_1 \frac{R_{obs}}{R_{obs\max}} + w_2 \left(1 - \frac{P_{dis}}{\sum_{i=1}^{k} P_{dis}} \right) \tag{15}$$

The obstruction degree of the obstacle constructed is determined by the radius R_{obs} of the obstacle and the maximum influence radius $R_{obs\max}$ of obstacles. As shown in Figure 5a, the larger the impact range of an obstacle, the more valuable it is for path planning. Equation (16) is constructed to describe the degree of dispersion P_{dis} between the obstacle and other obstacles. The denser the distribution of obstacles in the environment, the lower the benefits of removing obstacles. As shown in Figure 5b, the distribution of R_2 is relatively sparse. It is considered that clearing R_2 is more effective in improving the quality of path planning than clearing R_1.

$$P_{dis} = \begin{cases} \overline{d}_f - \frac{\sqrt{\sum_{j=1}^{m} \left(d_f^{R_j} - \overline{d}_f \right)^2}}{m}, \ 2 \le m < k \\ \overline{d}_f, \ m = 1 \\ 0, m = 0 \end{cases} \tag{16}$$

where f is the line segment equation between the current obstacle and the flight endpoint, $d_f^{R_j}$ represents the distance from obstacle j to the line, and m represents the number of obstacles that are close to the current obstacle ($d_f^{R_j} < R_{obs}(j) + \varepsilon$) and closer to the flight endpoint than the current obstacle.

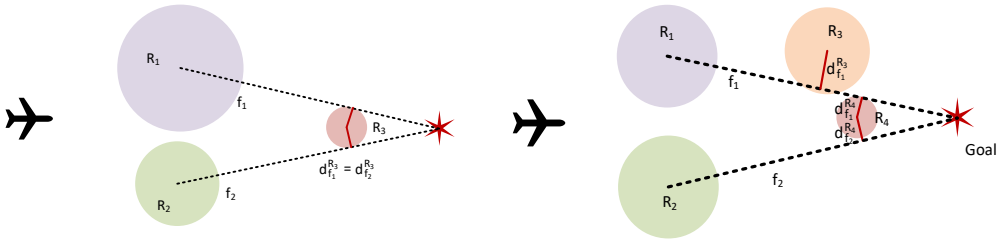

(**a**) (**b**)

Figure 5. Benefits of obstacle clearance: (**a**) the influence of obstacle radius and (**b**) the influence of obstacles distribution.

Based on the above analysis, state observations are obtained based on the interaction between the drone and obstacle environments and are defined as follows:

$$S_i = \begin{pmatrix} \Delta x_i, \Delta y_i, \Delta z_i, \Delta d_{x_i}, \Delta d_{y_i}, \Delta d_{z_i}, \Delta v_{xi}, \Delta v_{yi}, \Delta v_{zi}, r_{cro}, r_{atts}, r_{attv}, \\ R_{obs}(i), \chi, \gamma, q, \Delta x'_j, \Delta y'_j, \Delta z'_j, P_{oi} \end{pmatrix} \tag{17}$$

where $\Delta x_i, \Delta y_i, \Delta z_i$ are the relative positions of the drone and the nearest obstacle; $\Delta d_{x_i}, \Delta d_{y_i}$, Δd_{z_i} are the relative positions of the nearest obstacle to the end point; $\Delta v_{xi}, \Delta v_{yi}, \Delta v_{zi}$ are the relative velocity amplitude of the drone and the nearest obstacle; χ, γ are respectively the heading angle and climb angle of the drone, q represents the remaining cost of obstacle clearing for the drone, $\Delta x'_j, \Delta y'_j, \Delta z'_j$ are the relative positions of the nearby obstacle j and the drone, and P_{oi} represents the position information of obstacle i at seven historical moments.

4.3. Construction of a Comprehensive Reward Mechanism

In order to improve the learning efficiency of action strategies and the exploration ability of global optimal solutions, a comprehensive reward mechanism was constructed, which includes dense instant reward and sparse ultimate reward.

4.3.1. The Instant Reward

The instant reward is reflected in the state of the drone, so it can provide immediate feedback to guide the agent to carry out the optimal action at each time step. The calculation formula is shown in Equation (18), including r_{ft}, r_{col}, and r_h. The specific analysis is as follows:

$$r_{in} = \frac{3}{5} r_{ft} + \frac{2}{5} r_{col} + r_h \tag{18}$$

(1) Flight tendency reward r_{ft}: This represents the distance from the next point planned by the drone to the destination. A longer distance indicates that the drone has a trend of gradually approaching the destination, resulting in a shorter path length and a greater reward value.

$$r_{ft} = \frac{\left\| P_{uav}(t+1) - P_{goal} \right\| - \left\| P_{uav}(t) - P_{goal} \right\|}{L_{\max}} \tag{19}$$

(2) Flight safety reward r_{col}: This is determined by the distance between the drone and the surface of the obstacle. The farther the distance from the obstacle, the longer the path length will inevitably be. Therefore, the flight safety threshold dis_{st} was set. When the distance from the obstacle surface is less than dis_{st}, the corresponding punishment will be given. r_{col} is calculated as follows:

$$r_{col} = \begin{cases} a, \ if \ dis^O_{uav} \geq dis_{st} \\ \frac{dis^O_{uav} - dis_{st}}{dis_{st}}, \ if \ dis^O_{uav} < dis_{st} \end{cases} \tag{20}$$

where $dis^O_{uav} = \| P_{uav} - P_{obs} \| - R_{obs}$, and $\| P_{uav} - P_{obs} \|$ is the distance between the drone and the center of the obstacle.

(3) Border security reward r_h: In order to avoid the problem of the drone being unable to effectively learn parameters by adjusting its flight height to too high or too low, it is necessary to set boundary safety thresholds z_{t1} and z_{t2}, and impose the corresponding punishment when the flying altitude is low or high. The calculation formula is as follows:

$$r_h = \begin{cases} \frac{e^{(Z_{uav}-Z_{\min})/z_{t1}}}{e-1} - 1, \ if \ Z_{uav} - Z_{\min} < z_{t1} \\ \frac{e^{(Z_{\max}-Z_{uav})/z_{t2}}}{e-1} - 1, \ if \ Z_{\max} - Z_{uav} < z_{t2} \end{cases} \tag{21}$$

4.3.2. The Ultimate Reward

At the end of the episode, the instant reward is disabled, and the ultimate reward is returned based on the status of the planning result to help the agent plan and make decisions for long-term goals. The final state is divided into four situations:

Situation 1: When the drone successfully reaches the end, it receives a reward for completing the planned mission. The calculation of the reward is shown in Equations (22) and (23).

$$r_{end} = pen_0\left(\frac{r_{len}}{2} + \frac{r_v}{4} + \frac{r_{ang}}{4} + r_{co}\right) \tag{22}$$

$$r_{len} = \frac{L_{\min}}{L_{path}}, r_v = -\frac{\sum_{i\in(1,N)} \left|v_i - \overline{v}\right| \Big/ N}{\Delta v_{\max}}, r_{ang} = \frac{1}{2}\left(1 - \frac{\sum_{n=1}^{N-1} \left|\dot{\chi}_{n+1} - \dot{\chi}_n\right|}{(N-1)\dot{\chi}_{\max}}\right) + \frac{1}{2}\left(1 - \frac{\sum_{n=1}^{N-1} \left|\dot{\gamma}_{n+1} - \dot{\gamma}_n\right|}{(N-1)\dot{\gamma}_{\max}}\right) \tag{23}$$

where L_{path} is the total length of the path. $\overline{v}$ is the average flight speed. $\left|\dot{\chi}_{n+1} - \dot{\chi}_n\right|$ and $\left|\dot{\gamma}_{n+1} - \dot{\gamma}_n\right|$ represent the variation in flight angles within an adjacent sampling interval.

In addition, when the drone performs an obstacle-clearing action, the corresponding additional action reward r_{co} is given. The reward calculation formula is as follows, where M represents the number of obstacles cleared.

$$r_{co} = \frac{10 \sum_{m=1}^{M} r_{attv}(m) r_{atts}(m)}{M} \tag{24}$$

Situation 2: When the drone hits an obstacle, the episode ends and the drone receives a punishment. In order to improve the search ability of the action s, the punishment is set to be related to the position of the drone at the moment T_{end}, as shown in Equation (25).

$$r_{end} = -pen_1 \frac{\left\| P_{uav}(T_{end}) - P_{goal} \right\|}{L_{\min}} \tag{25}$$

Situation 3: When the q of the drone is less than 0, this indicates that the drone has carried out too many clearing obstacle operations. The learning of this episode is over, and the drone receives the corresponding punishment. The calculation method of punishment is similar to Equation (25).

Situation 4: When the drone flies out of the airspace, the corresponding punishment is obtained, and the calculation method of punishment is similar to Equation (25).

pen_0 and pen_1 are the final reward coefficients, and they are set to $\frac{2}{3} \times Step_{\max}$, where $Step_{\max}$ is the maximum time step. The reason for this is to avoid the drone focusing too much on instant rewards and ignoring the long-term path planning goal.

4.4. Learning of Obstacle-Avoidance Strategies Based on the PDQN-IFDS

4.4.1. The Structure of the PDQN-IFDS

The angle adjustment of the drone involves learning two continuous parameters: climbing angle and heading angle. It is necessary to find the optimal combination of continuous parameters, which causes the problem of difficult convergence of the algorithm

and poor path planning quality. When the IFDS is introduced, the parameters of angles become ρ, σ, and θ. The three parameters are closely related to the position of the drone and the position and radius of obstacles, and they determine the direction, shape, and avoidance time of path planning.

$$\begin{cases} \chi_c = \tan^{-1}\left(\frac{\overline{u}_y}{\overline{u}_x}\right) \\ \gamma_c = \sin^{-1}\left(\frac{\overline{u}_z}{\|\overline{u}(P)\|}\right) \end{cases} \tag{26}$$

The PDQN is used to train the probability distribution of parameters to guide the learning of climb angle and heading angle, as shown in Equation (26), so as to effectively improve the learning efficiency of obstacle-avoidance strategies.

The PDQN-IFDS is divided into four neural networks, namely ParamActorNet, Q-Net, ParamActor-TargetNet, and Q-TargetNet. The structure of ParamActorNet is divided into four layers, with network nodes of 40, 128, 256, and 5, respectively. The 40 nodes of the input layer correspond to the size of the state space (Equation (17)). The number of output nodes corresponds to the 5 parameters of the hybrid action space. $a \in [-15, 15]\mathrm{m/s}^2$, $\rho_k \in [1, 5]$, $\sigma_k \in [1, 5]$, $\theta_k \in [0, \pi]$, and remove is 0/1. Each parameter is normalized to [−1,1], which avoids the problems of inconsistent convergence speed and gradient instability. The structure of Q-net is still divided into four layers, and the corresponding network nodes are 45, 128, 256, and 3. The number of output nodes corresponds to three different obstacle-avoidance decisions: adjusting angles, adjusting speed, and obstacle clearance. ParamActor-TargetNet and Q-TargetNet are obtained by copying parameters from ParamActorNet and Q-Net.

4.4.2. The Training Process of the PDQN-IFDS

Based on the loss function of the PDQN-IFDS in Section 3.1, the gradient of $L_t^Q(w)$ on the Q-Net network parameter w can be expressed as Equation (27), and w is updated via the gradient descent method: $w \leftarrow w - \alpha_1 \nabla_w L_t^Q$, where α_1 is the learning rate.

$$\nabla_w L_t^Q = \left(y_t - Q\left(s_t, k_t, x_{k_t}|w\right)\right) \nabla_w Q\left(s_t, k_t, x_{k_t}|w\right) \tag{27}$$

ParamActorNet is designed to maximize the cumulative expected return, and θ is updated by policy gradients: $\theta \leftarrow \theta - \alpha_2 \nabla_\theta L_t^\pi$.

$$\nabla_\theta L_t^\pi = -\sum_{k=1}^{K} \nabla_x Q(s_t, k, x_k(s_t|\theta)|w_t) \nabla_\theta x(s|\theta) \tag{28}$$

The soft update is adopted for ParamActor-TargetNet and Q-TargetNet, as shown in Equation (29).

$$\theta' \leftarrow \tau_1 \theta + (1 - \tau_1)\theta', w' \leftarrow \tau_2 w + (1 - \tau_2) w' \tag{29}$$

4.5. MSAO2H Model

We designed the random obstacle environments in the development framework of OpenAI Gym 0.10.5. According to the introduction in Sections 4.1–4.4, the interaction process of the four parts is shown in Figure 6: By inputting the real-time status of the drone and the obstacle environment (Section 4.1) into the PDQN-IFDS (Section 4.4), the drone learns the best obstacle avoidance strategies (Section 4.2) under the guidance of the reward mechanism (Section 4.3), so as to complete a sequential decision process of path planning.

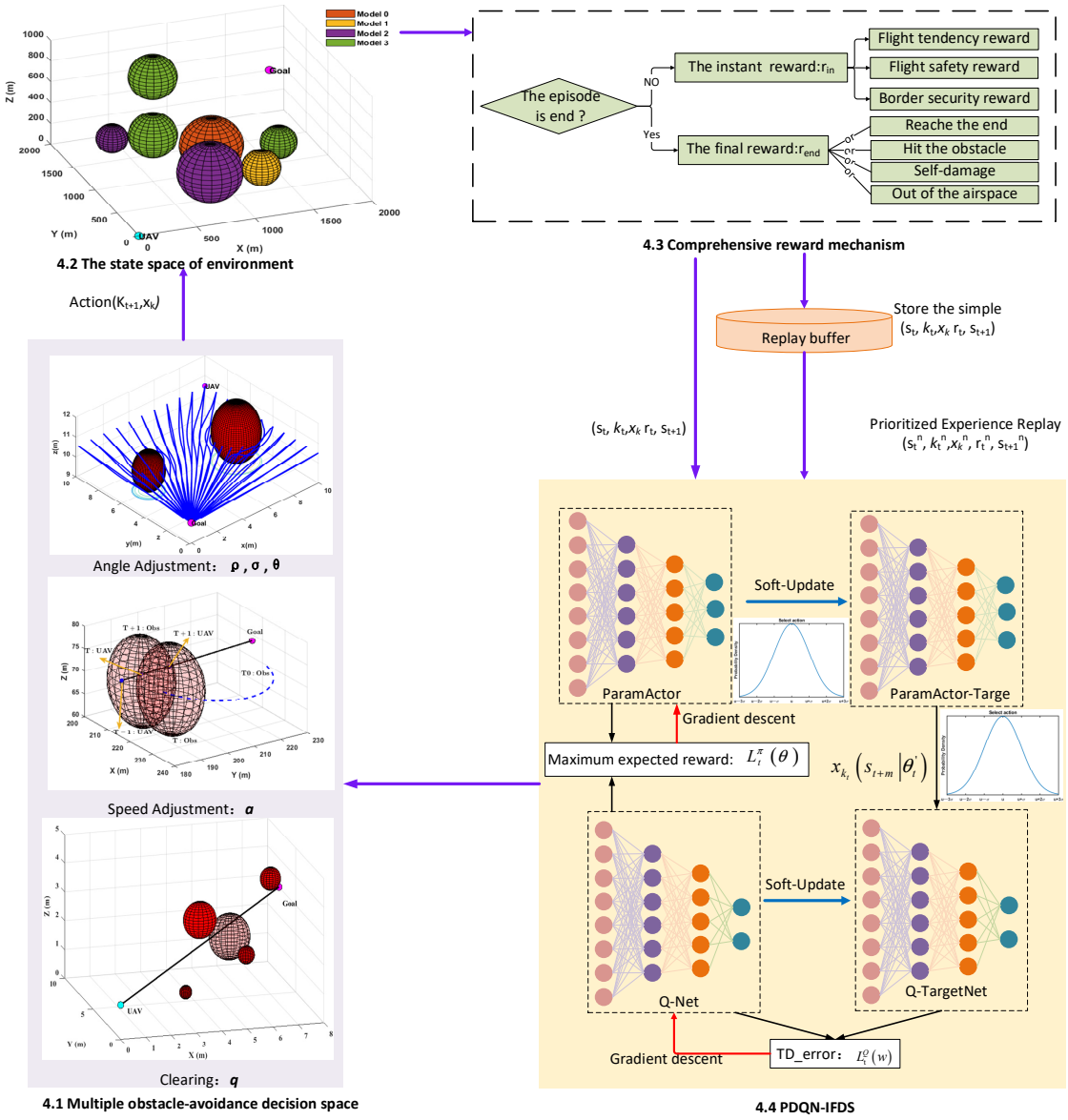

Figure 6. Flow chart of the autonomous path planning algorithm of drones based on MSAO2H.

The MSAO2H model training process is shown in Algorithm 1:

Algorithm 1: The training process of MSAO2H

Initialization: Randomly initialize w,θ, targrt nets $\theta\prime \leftarrow \theta; w\prime \leftarrow w$; Replay memory D;
for episode ⟵ 1 to Max **do**
  for step t ⟵ 1 to TMax or *IsDone* **do**
    Obtain initial state: S (by Equations (14)–(17));
    Execute the action $a_t(k_t, x_t)$ (by Equations (11)–(13) and (26));
    Obtain reward r and new state S_{t+1} (by Equations (18)–(25));
    Update step counters: $t \leftarrow t + 1$;
    Store the simple (s_t, a_t, r_t, s_{t+1}) in D;
    Obtain random a batch of (s_t, a_t, r_t, s_{t+1}) from D;
    Update ParamActorNet, Q-Net, ParamActor-TargetNet, Q-TargetNet (by Equations (27)–(29)).
  end for
end for

5. Simulation Experiment and Analysis

We designed obstacle environments in the OpenAI Gym 0.10.5 development framework for autonomous path planning of the drone. Through the interaction between the drone and the obstacles, data were collected. As a random environment, at the episode end of obstacle avoidance tasks, obstacles in the airspace will be reinitialized randomly. Considering the motion constraints of the drone, the climbing angle of the drone was set to $\eta \in (-25°, 25°)$ and the speed was set to $v_d \in [30, 80]$m/s. The time step was 20 s, and the maximum changes in the heading angle and climb angle of the drone at each step were 15° and 8°, respectively. This paper analyzes the impact of the proposed method on path planning from two perspectives:

(1) In the random training environments, the average success rate and average reward of the deep deterministic policy gradient (DDPG), DDPG-IFDS, PDQN, and MSAO2H are compared to verify the effectiveness of the diversified obstacle-avoidance decisions.

(2) We compared the results based on different methods in test environments to verify the versatility of MSAO2H.

5.1. Analysis of Effectiveness

The training convergence results of the DDPG, DDPG-IFDS, PDQN, and MSAO2H during training were compared. The DDPG and DDPG-IFDS only adjust the climbing angle and heading angle of the drone for route planning. PDQN and MSAO2H perform route planning by making three types of obstacle-avoidance decisions: adjusting angles, adjusting speed, and clearing obstacles. The DDPG-IFDS and MSAO2H learn the parameters of angle adjustment based on the IFDS algorithm. In the training process, the ε-greedy algorithm [39] was adopted, with the initial value ε of 0.9, gradually decreasing to 0.01 as the number of iterations increases. The parameters of the PDQN are shown in Table 1.

Table 1. Parameter settings of the PDQN.

Parameter	Discount Factor	Learning Rate		Smoothing Factor		Batch Size
	γ	α_1	α_2	τ_1	τ_2	
Value	0.9	0.001	0.0001	0.001	0.1	256

The number of training iterations was set to 4 million times, and the average reward and average success rate were calculated every 1000 iterations. The training convergence results of the four models are shown in Figure 7.

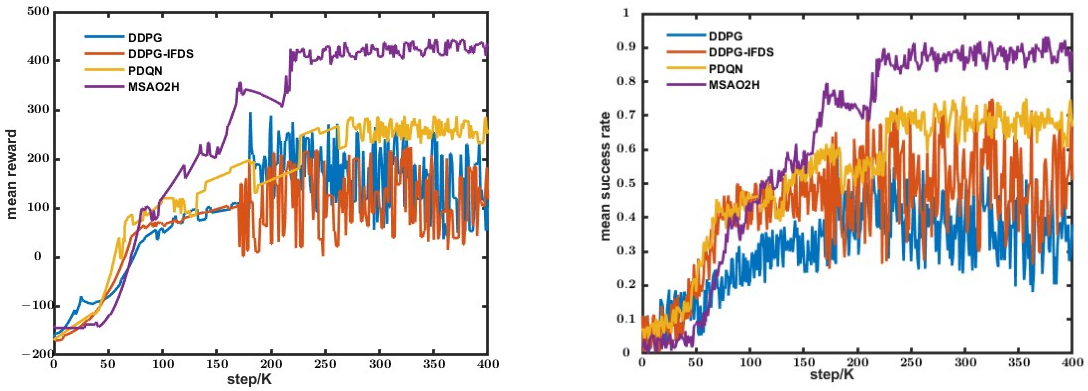

(**a**) (**b**)

Figure 7. The convergence iteration results based on different networks: (**a**) the convergence of average reward and (**b**) the convergence of average success rate.

Due to there being fewer parameters of obstacle avoidance action in the DDPG and DDPG-IFDS, they exhibit faster convergence speeds compared to the algorithms based

on hybrid action space. However, the convergence average reward and convergence average success rate are lower. Additionally, the average reward value and average success rate fluctuate greatly, indicating that these two models are highly sensitive to obstacle environments and difficult to apply widely. The average reward during the initial stage of PDQN training (0–100 K iterations) increases more rapidly than that of MSAO2H. But the PDQN shows a slower increase in rewards during the later stages. After 260 K iterations of training, the PDQN gradually converged. The average reward and average success rate after convergence are lower than those of MSAO2H. This suggests that the avoidance decisions learned from the PDQN have certain limitations. Although the average reward and average success rate of MSAO2H are low in the initial learning stage, after 220 K iterations, the average reward converges to a high value, and the average success rate converges to 0.92. The main reason for the phenomenon is that the model transforms challenging-to-learn parameters into parameters related to the relative position and radius of the nearest obstacle. This physical interpretation can help to comprehend angle adjustments and improve the learning efficiency of obstacle-avoidance actions.

The training results, based on the random obstacle environments, show that the proposed method can effectively complete the avoidance tasks, and the proposed model demonstrates a certain level of generalization.

5.2. Analysis of Versatility

5.2.1. Analysis of Planning Results in Simple Obstacle Environments

We compared the path planning results based on Astar, the IFDS, rapidly-exploring random tree (RRT), DDPG, DDPG-IFDS, PDQN, and MSAO2H in the airspace of 12 static obstacles, as shown in Figure 8.

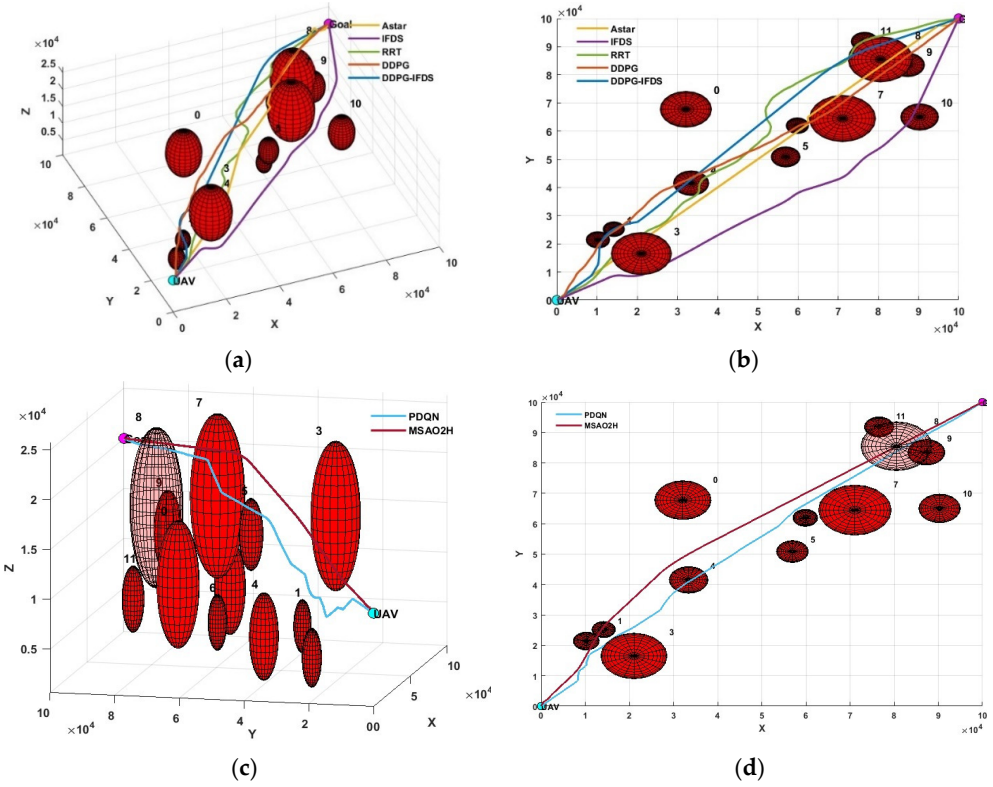

Figure 8. Result of path planning in a simple environment: (**a**) The three-dimensional paths based on Astar, the IFDS, RRT, DDPG, and DDPG-IFDS; (**b**) the two-dimensional results based on Astar, the IFDS, RRT, DDPG, and DDPG-IFDS; (**c**) the three-dimensional paths based on the PDQN and MSAO2H; (**d**) the two-dimensional results based on the PDQN and MSAO2H.

The angles of the drone and their variation are shown in Figure 9. The trend of the distance from the nearest obstacle during flight is shown in Figure 10. Table 2 shows the P_p, C_p, and D_p of the paths obtained by seven algorithms.

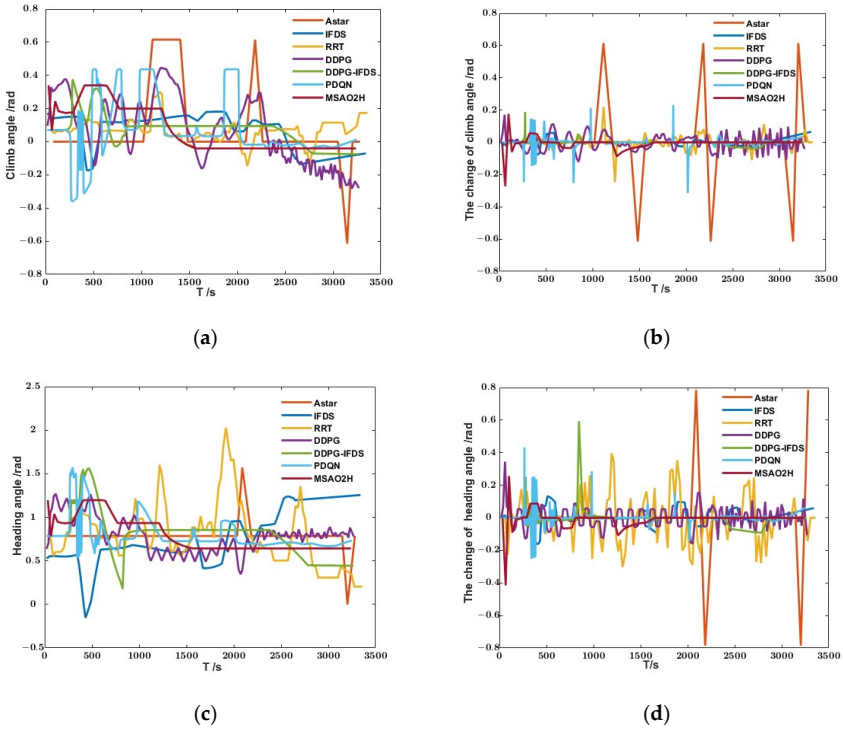

Figure 9. The change in the flight angle of the drone: (**a**) the climb angle of the drone; (**b**) the climb change rate of the drone; (**c**) the heading angle of the drone; (**d**) the heading change rate of the drone.

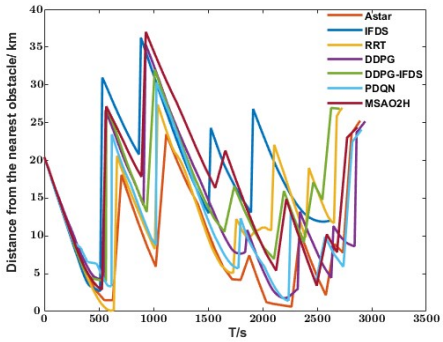

Figure 10. The variation in the distance of the drone to the nearest obstacle.

Table 2. Evaluation results of planning paths in a simple environment.

	Astar	**IFDS**	**RRT**	**DDPG**	**DDPG-IFDS**	**PDQN**	**MSAO2H**
P_p/m	147,653	150,329	151,162	147,179	146,920	146,101	145,770
C_p	0.0922	0.0537	0.0603	0.0854	0.0541	0.0939	0.0480
D_p/m	638	2690	93	1750	4030	1400	2265

Compared with Figures 9 and 10, it can be observed from the path planning results based on Astar that the climb angle of the drone and its variation amplitude exceed the constraint conditions, resulting in low path smoothness and falling into the local optimal solution. Due to the random sampling and exploration method of the RRT, the climbing angle and heading angle fluctuate significantly, leading to a longer planned path length.

Furthermore, the closest distance to the obstacle surface is 93 m, indicating a low level of path safety and poor overall path planning quality. Compared to the RRT and Astar, the path planning results based on the IFDS show a safe distance from obstacles, as well as more gradual changes in climb angle and heading angle. The resulting path is smoother, but the quality of the path depends on the hyperparameter settings. The planning result is based on the IFDS with $\rho = 1$, $\sigma = 1$, and $\theta = 0.1$.

By using deep reinforcement learning to learn the distribution of hyperparameters in the IFDS, it is possible to dynamically adjust parameters for various obstacles and improve adaptive capabilities. As shown in Table 2, the path planned by the DDPG-IFDS exhibits similar tortuosity compared to the IFDS model. It maintains a longer distance from the obstacle surface (the nearest distance is 1400 m) while reducing the length of the path planning result by 2.81%. The length and tortuosity of the path based on MSAO2H were reduced by 3.03% and 10.62%, respectively.

In the planning results based on hybrid action networks (PDQN and MSAO2H), obstacle 8 is cleared. According to Table 2, it can be seen that the planned path is significantly shortened compared to the DDPG and DDPG-IFDS. Therefore, the obstacle clearance decision represents a more optimal solution. Although the PDQN and DDPG reduce the path length to a certain extent, it can be seen from Figure 10 that both of them have the problem of significant fluctuations in the climb angle, resulting in poor path smoothness.

As shown in Table 2, the path generated by MSAO2H has the shortest length, the lowest degree of tortuosity, and a safe distance from the nearest obstacle, resulting in higher comprehensive path planning quality. The results indicate that the proposed model achieves excellent performance.

5.2.2. Analysis of Planning Results in a Complex Obstacle Environment

Due to the lack of sensitivity to the perception of dynamic environments for traditional algorithms, it is difficult to respond promptly to the dynamic obstacles. In this paper, we compare the path planning results based on deep reinforcement network models in a dynamic obstacle environment. There are 21 obstacles in the simulated dynamic environment. Of them, 5 obstacles are static obstacles, 6 obstacles are in linear motion, 4 obstacles are in horizontal circular motion, and 6 obstacles are in serpentine motion. In this environment, the path planning results based on the DDPG, DDPG-IFDS, PDQN, and MSAO2H models are shown in Figures 11–14, respectively. To enhance the presentation of path planning results in the dynamic obstacle environment, only the time when each obstacle is closest to the drone, the corresponding position, and the path information of the closest obstacle in a short time are exclusively highlighted in Figures 11–14. The change in the relative distance to the nearest obstacle during flight is shown in Figure 15. Similarly, P_p, C_p, and D_p of the paths are shown in Table 3.

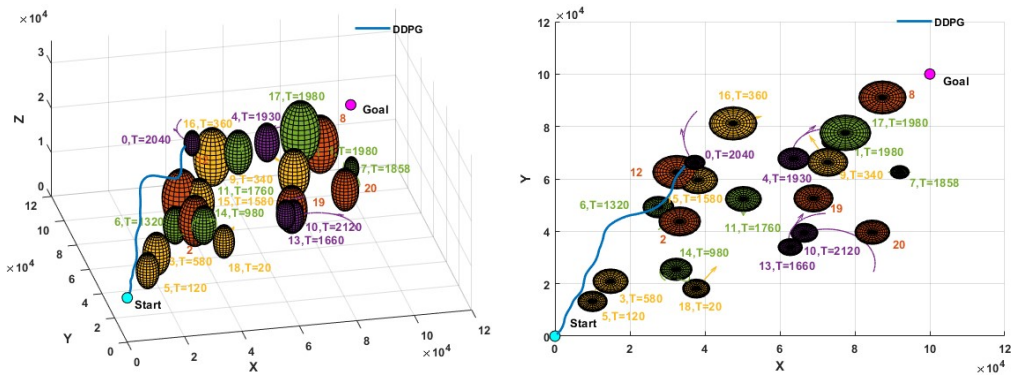

(**a**) (**b**)

Figure 11. Result of path planning based on the DDPG in a complex environment: (**a**) three-dimensional path and (**b**) X-Y plane projection.

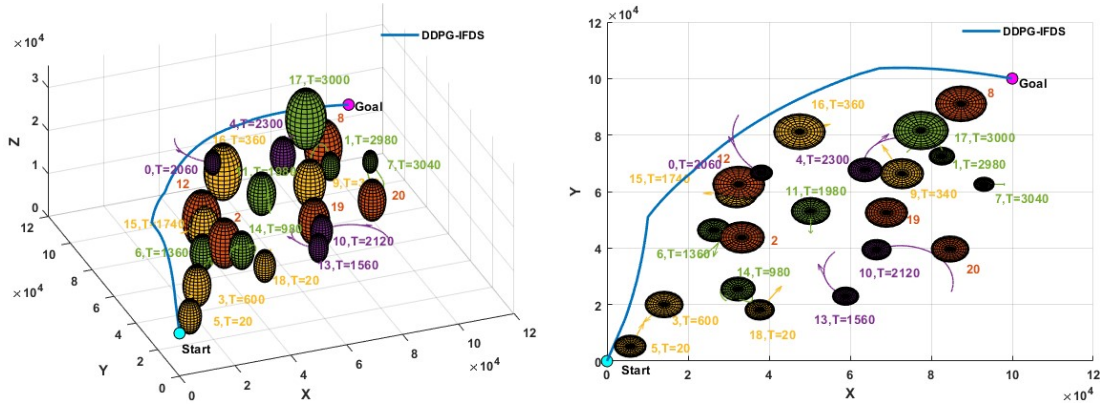

(**a**) (**b**)

Figure 12. Result of path planning based on the DDPG-IFDS in a complex environment: (**a**) three-dimensional path and (**b**) X-Y plane projection.

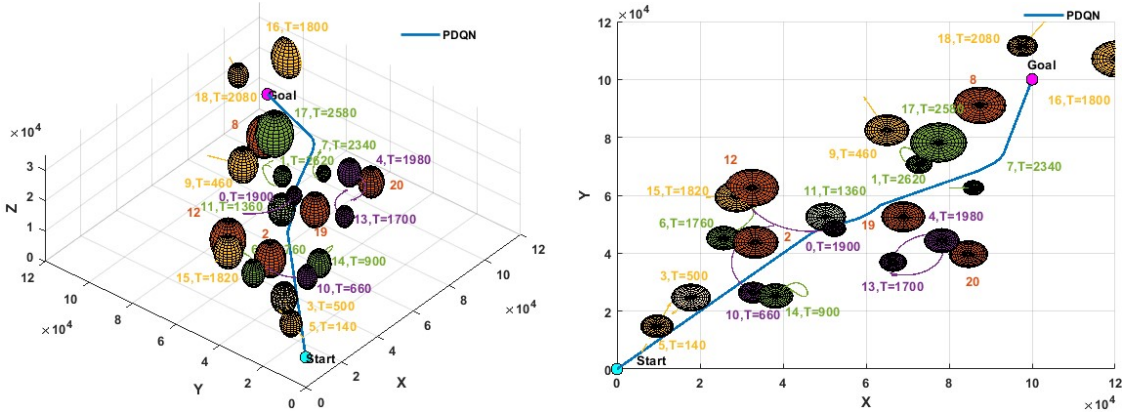

(**a**) (**b**)

Figure 13. Result of path planning based on the PDQN in a complex environment: (**a**) three-dimensional path and (**b**) X-Y plane projection.

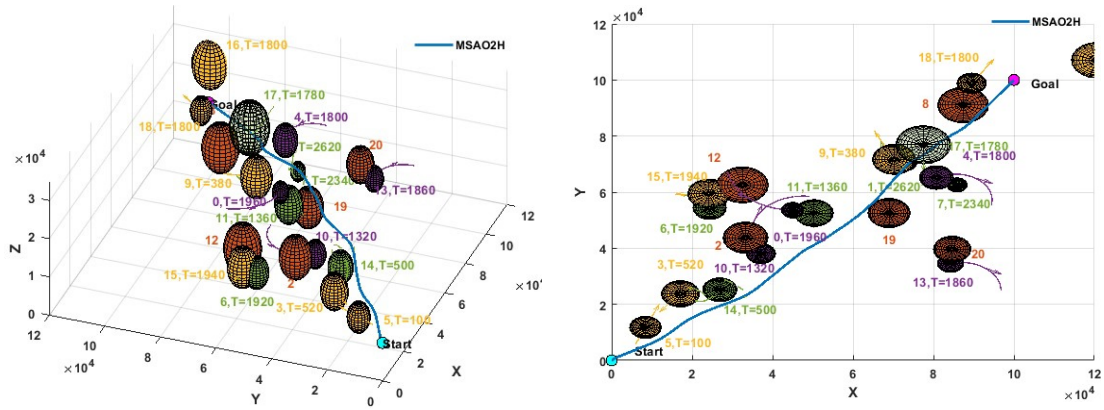

(**a**) (**b**)

Figure 14. Result of path planning based on MSAO2H in a complex environment: (**a**) three-dimensional path and (**b**) X-Y plane projection.

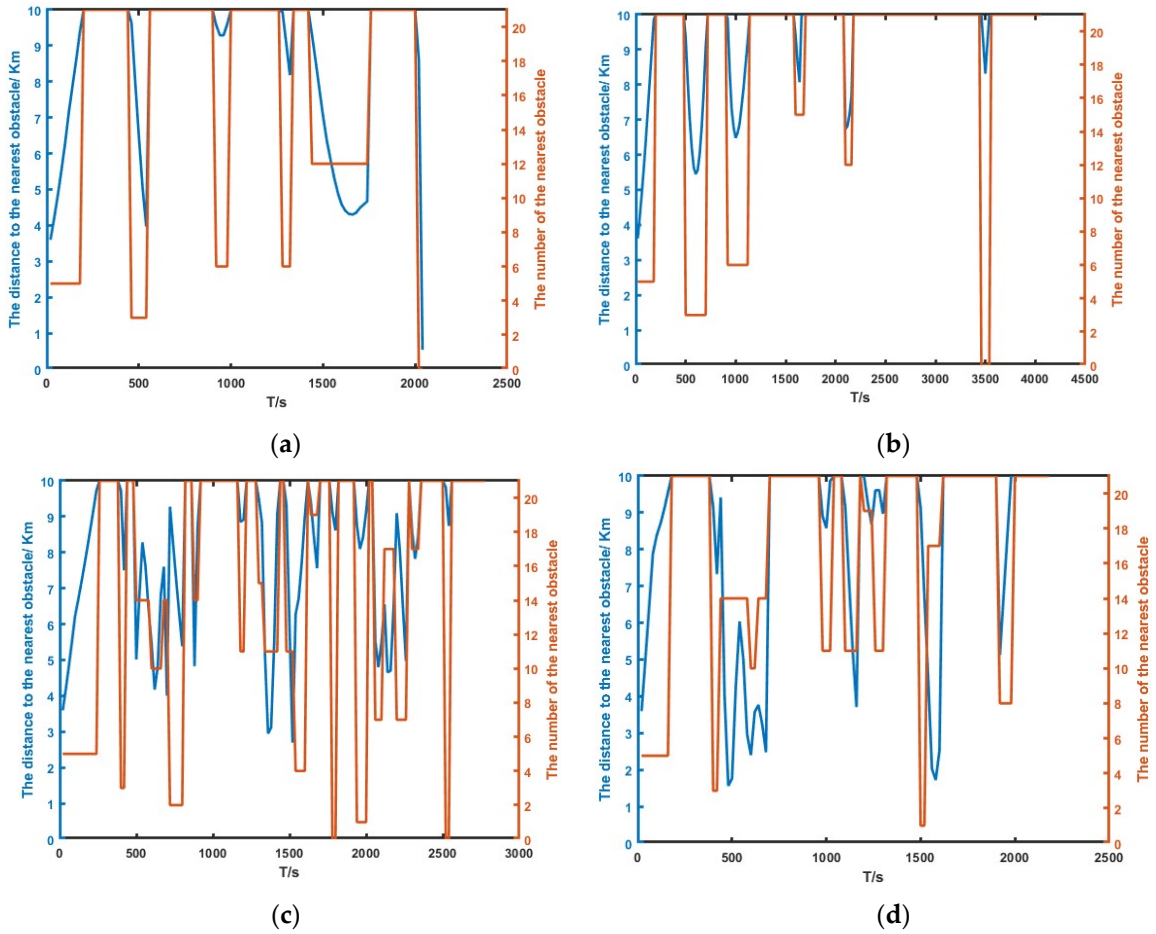

Figure 15. Distance to the nearest obstacle during flight; (**a**) based on the DDPG; (**b**) based on the DDPG-IFDS; (**c**) based on the PDQN; (**d**) based on MSAO2H.

Table 3. Evaluation results of planning paths in a complex dynamic environment.

	DDPG	DDPG-IFDS	PDQN	MSAO2H
P_p/m	-	165,946	148,491	146,082
C_p	-	0.1453	0.0788	0.0705
D_p/m	-	3617	2694	1563

As shown in Figure 11, the DDPG model failed to avoid obstacle 0. In contrast, the paths of the other three models were successfully planned. The results in Figures 13 and 14 show that th ePDQN and MSAO2H can successfully plan a safe route in areas with a dense obstacle distribution based on three obstacle avoidance decisions. The difference is that PDQN clears obstacles 3 and 17, while MSAO2H only clears obstacle 17, and the clearing cost based on MSAO2H is lower.

In addition, we analyzed the changes in the relative distance between the drone and the nearest obstacle during flight, as shown in Figure 15. The horizontal axis represents the flight time of the drone. The blue line on the left vertical axis represents the relative distance between the drone and the nearest obstacle. The red line on the right vertical axis represents the number of the nearest obstacle (0–20 represents the number of the 21 obstacles; 21 means no obstruction within 10 km).

According to Figure 15a, the DDPG fails to avoid obstacle 0 at $t = 2040$ resulting in the failure of path planning. It can be seen from Figure 15b that the distance between the drone and obstacles is relatively far on the whole. According to Figure 12, the main reason for the phenomenon is that the DDPG-IFDS is planned in areas with a relatively wide distribution

of obstacles, which causes the path length to be too large (the length is 165,946 m). The number of the nearest obstacle changes rapidly as shown in Figure 15c,d, indicating that the PDQN and MSAO2H can be applied to complex obstacle environments with high dynamics. Compared with Figure 15c, the change in the number of nearest obstacles is slower and the average distance from the nearest obstacle is longer in Figure 15d. This suggests that the path planned based on the MSAO2H model is more secure.

As shown in Table 3, compared with the results of path planning under the obstacle environment in Section 5.2.1, the path length increases and the smoothness decreases in the dynamic environment. However, the path planned based on MSAO2H still has the shortest length and the highest smoothness and maintains a certain safety range with obstacles, resulting in the highest quality of planned paths. The length and tortuosity of the path obtained by MSAO2H are 1.62% and 10.55% lower than those obtained by the PDQN, respectively. This result indicates that the obstacle-avoidance decisions learned by MSAO2H are more effective.

5.2.3. Analysis of Planning Results in Random Obstacle Environments

To further verify the versatility of MSAO2H, the performance of four models in 200 randomly generated obstacle environments was compared. We took 10 environments as a test set and calculated the average reward and average success rate of different models in each test set, as shown in Figure 16:

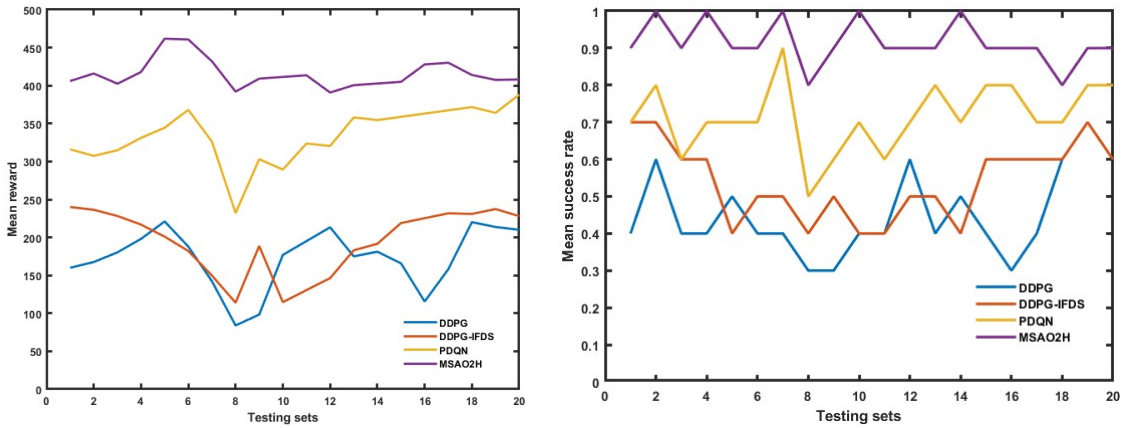

(**a**) (**b**)

Figure 16. Test results of path planning in random obstacle environments: (**a**) the average reward and (**b**) the average success rate.

Based on Figure 16, it is evident that the DDPG achieves its highest average reward of 221 in the fifth test set. The DDPG-IFDS surpasses this, attaining the highest average reward of 240 in the first test set. The PDQN outperforms both with a maximum average reward of 368 in the sixth test set. However, MSAO2H exhibits the most significant performance, securing the highest average reward of 461 in the fifth test set. The four models exhibit lower reward values in the eighth test set, with values of 84, 114, 232, and 392, respectively. Compared to the other models, MSAO2H demonstrates the smallest fluctuation in average reward in random testing environments. Additionally, the DDPG, DDPG-IFDS, and PDQN achieve their maximum success rates of 0.6, 0.7, and 0.9, respectively, in the test sets. Meanwhile, MSAO2H achieves the path success rate of one in five test sets, with a minimum success rate of 0.8 in the eighth set.

In 200 test environments, the average reward values of the four models are 173.19, 194.76, 335.09, and 415.456, and the average success rates are 0.45, 0.54, 0.715, and 0.915, respectively. These results indicate that MSAO2H has a higher average reward and success rate in the test environments, confirming the higher robustness of MSAO2H to the environment.

6. Conclusions

By constructing the state space of obstacle environments, various obstacle-avoidance strategies, a comprehensive reward mechanism, and the PDQN-IFDS, the MSAO2H model was constructed to achieve autonomous path planning for drones in dynamic and complex airspace environments. And compared with other methods, the effectiveness of the proposed method was verified:

(1) MSAO2H can continuously optimize the obstacle-avoidance decisions of drones based on feedback information from random dynamic obstacle environments. The average success rate of convergence and the average reward of convergence are high, which improves the autonomous capability of path planning and validates the generalization of the model.

(2) Compared to traditional path planning algorithms such as Astar, RRT, and IFDS, the proposed method has shorter and less tortuous degree planning results in the static obstacle environment while maintaining a safe distance from obstacle surfaces. The results have validated the fact that multiple obstacle avoidance decisions can effectively improve the quality of path planning.

(3) Compared with the DDPG and DDPG-IFDS, the proposed method can successfully plan routes in areas with dense obstacles. Compared with the PDQN, MSAO2H can converge more quickly and stably and plan high-quality paths. The results show that the proposed model makes path planning for drones in complex dynamic obstacle environments more reliable and efficient.

In this paper, deep reinforcement learning was used to study the global path planning method based on the motion constraints of drones. In the future, multi-agent reinforcement learning will be used to further study dynamic path planning under the constraints of autonomous navigation for formation and cluster cooperation.

Author Contributions: Conceptualization, F.Y.; methodology, T.Y. and D.L.; validation, T.Y.; formal analysis, T.Y., F.Y. and D.L.; data curation, T.Y. and D.L.; writing—original draft preparation, T.Y.; writing—Review and Editing, F.Y.; supervision, D.L.; funding acquisition, F.Y. All authors have read and agreed to the published version of the manuscript.

Funding: This research was funded by the Fundamental Research Program of Shanxi Province, grant No. 202203021221104, and the National Natural Science Foundation of China, grant No. 61972363.

Data Availability Statement: The data presented in this study are available from the corresponding author upon request.

Conflicts of Interest: The authors declare no conflicts of interest.

References

1. Zhou, C.; Gu, S.; Wen, Y. The review unmanned surface vehicle path planning: Based on multi-modality constraint. *Ocean Eng.* **2020**, *200*, 107043. [CrossRef]
2. Wu, X.; Xu, L.; Zhen, R.; Wu, X. Bi-directional adaptive A*algorithm toward optimal path planning for large-scale UAV under multi-constraints. *IEEE Access* **2020**, *8*, 85431–85440. [CrossRef]
3. Ren, Z.; Rathinam, S.; Choset, H. Multi-Objective Path-Based D* Lite. *IEEE Robot. Autom. Lett.* **2021**, *7*, 3318–3325. [CrossRef]
4. Niu, H.; Savvaris, A.; Tsourdos, A.; Ji, Z. Voronoi-visibility roadmap-based path planning algorithm for unmanned surface vehicles. *J. Navig.* **2019**, *72*, 850–874. [CrossRef]
5. Bashir, N.; Boudjit, S.; Dauphin, G.; Zeadally, S. An obstacle avoidance approach for UAV path planning. *Simul. Model. Pract. Theory* **2023**, *129*, 102815. [CrossRef]
6. Xu, X.; Zhang, F.F.; Zhao, Y. Unmanned Aerial Vehicle Path-Planning Method Based on Improved P-RRT* Algorithm. *Electronics* **2023**, *12*, 4576. [CrossRef]
7. Yuan, M.S.; Zhou, T.L.; Chen, M. Improved lazy theta* algorithm based on octree map for path planning of UAV. *Def. Technol.* **2023**, *23*, 8–18. [CrossRef]
8. Wang, S.; Lin, F.; Wang, T.; Zhao, Y.; Zang, L.; Deng, Y. Autonomous Vehicle Path Planning Based on Driver Characteristics Identification and Improved Artificial Potential Field. *Actuators* **2022**, *11*, 52. [CrossRef]
9. Celestini, D.; Primatesta, S.; Capello, E. Trajectory Planning for UAVs Based on Interfered Fluid Dynamical System and Bézier Curves. *IEEE Robot. Autom. Lett.* **2022**, *7*, 9620–9626. [CrossRef]

10. Wu, J.; Wang, H.; Zhang, M. On obstacle avoidance path planning in unknown 3D environments: A fluid-based framework. *ISA Trans.* **2020**, *111*, 249–264. [CrossRef]
11. Hao, G.Q.; Lv, Q.; Huang, Z.; Zhao, H.L.; Chen, W. UAV Path Planning Based on Improved Artificial Potential Field Method. *Aerospace* **2023**, *10*, 562. [CrossRef]
12. Diao, Q.; Zhang, J.; Liu, M.; Yang, J. A Disaster Relief UAV Path Planning Based on APF-IRRT* Fusion Algorithm. *Drones* **2023**, *7*, 323. [CrossRef]
13. Goricanec, J.; Milas, A.; Markovic, L.; Bogdan, S. Collision-Free Trajectory Following With Augmented Artificial Potential Field Using UAVs. *IEEE Access* **2023**, *11*, 83492–83506. [CrossRef]
14. Hao, Z.; Xiong, H.L.; Liu, Y. Trajectory Planning Algorithm of UAV Based on System Positioning Accuracy Constraints. *Electronics* **2020**, *9*, 250. [CrossRef]
15. Phung, M.D.; Hao, P. Safety-enhanced UAV path planning with spherical vector-based particle swarm optimization. *Appl. Soft Comput.* **2021**, *2*, 107376. [CrossRef]
16. Miao, C.; Chen, G.; Yan, C. Path planning optimization of indoor mobile robot based on adaptive ant colony algorithm. *Comput. Ind. Eng.* **2021**, *156*, 107230. [CrossRef]
17. Hu, K.; Mo, Y. A novel unmanned aerial vehicle path planning approach: Sand cat optimization algorithm incorporating learned behaviour. *Meas. Sci. Technol.* **2024**, *35*, 046203. [CrossRef]
18. Zhou, X.J.; Tang, Z.H.; Wang, N.; Yang, C.H.; Huang, T.W. A novel state transition algorithm with adaptive fuzzy penalty for multi-constraint UAV path planning. *Expert Syst. Appl.* **2024**, *248*, 123481. [CrossRef]
19. Wu, X.J.; Xu, L.; Zhen, R.; Wu, X.L. Global and Local Moth-flame Optimization Algorithm for UAV Formation Path Planning Under Multi-constraints. *Int. J. Control. Autom. Syst.* **2023**, *21*, 1032–1047. [CrossRef]
20. Ji, M.; Zhang, L.; Wang, S. A Path Planning Approach Based on Q-learning for Robot Arm. In Proceedings of the 2019 3rd International Conference on Robotics and Automation Sciences (ICRAS), Wuhan, China, 1–3 June 2019.
21. Chen, C.; Chen, X.Q.; Ma, F. A knowledge-free path planning approach for smart ships based on reinforcement learning. *Ocean Eng.* **2019**, *189*, 106299. [CrossRef]
22. Hao, B.; Du, H.; Yan, Z.P. A path planning approach for unmanned surface vehicles based on dynamic and fast Q-learning. *Ocean Eng.* **2023**, *270*, 113632. [CrossRef]
23. Qian, S.; Lam, H.K.; Xuan, C.B.; Chen, M. Adaptive neuro-fuzzy PID controller based on twin delayed deep deterministic policy gradient algorithm. *Neurocomputing* **2020**, *402*, 183–194.
24. Tao, Y.; Zhang, W.A.; Simon, X.; Yang, L.Y. Soft Actor-Critic Reinforcement Learning for robotic manipulator with Hindsight Experience Replay. *Int. J. Robot. Autom.* **2019**, *34*, 536–543.
25. Li, Y.; Zhang, S.; Ye, F. A UAV Path Planning Method Based on Deep Reinforcement Learning. In Proceedings of the 2020 IEEE USNC-CNC-URSI North American Radio Science Meeting (Joint with AP-S Symposium), Toronto, ON, Canada, 5–10 July 2020.
26. Zhang, S.; Li, Y.; Dong, Q. Autonomous navigation of UAV in multi-obstacle environments based on a Deep Reinforcement Learning approach—ScienceDirect. *Appl. Soft Comput.* **2021**, *115*, 115.
27. Wang, C.; Wang, J.; Wang, J. Deep Reinforcement Learning-based Autonomous UAV Navigation with Sparse Rewards. *IEEE Internet Things J.* **2020**, *7*, 6180–6190. [CrossRef]
28. Tang, J.; Liang, Y.; Li, K. Dynamic Scene Path Planning of UAVs Based on Deep Reinforcement Learning. *Drones* **2024**, *8*, 60. [CrossRef]
29. Yan, C.; Xiang, X.; Wang, C. Towards Real-Time Path Planning through Deep Reinforcement Learning for a UAV in Dynamic Environments. *J. Intell. Robot Syst.* **2020**, *98*, 297–309. [CrossRef]
30. Zhou, Y.X.; Shu, J.S.; Hao, H.; Song, H.; Lai, X.C. UAV 3D online track planning based on improved SAC algorithm. *J. Braz. Soc. Mech. Sci. Eng.* **2023**, *46*, 12. [CrossRef]
31. Luo, X.Q.; Wang, Q.Y.; Gong, H.F.; Tang, C. UAV Path Planning Based on the Average TD3 Algorithm With Prioritized Experience Replay. *IEEE Access* **2021**, *12*, 38017–38029. [CrossRef]
32. Zhou, F.; Rui, S.; Zhang, W. Hybrid Actor-Critic Reinforcement Learning in Parameterized Action Space. *arXiv* **2019**, arXiv:1903.01344. [CrossRef]
33. Xu, Y.H.; Wei, Y.R.; Jiang, K.Y.; Chen, L.; Wang, D.; Deng, H.B. Action decoupled SAC reinforcement learning with discrete-continuous hybrid action spaces. *Neurocomputing* **2023**, *537*, 141–151. [CrossRef]
34. Chen, S.Q.; Su, R. An autonomous agent for negotiation with multiple communication channels using parametrized deep Q-network. *Math. Biosci. Eng.* **2022**, *19*, 7933–7951. [CrossRef]
35. Bester, C.J.; James, S.D.; Konidaris, G.D. Multi-Pass Q-Networks for Deep Reinforcement Learning with Parameterised Action Spaces. *arXiv* **2019**, arXiv:1905.04388. [CrossRef]
36. Huang, C.; Zhang, H.; Wang, L. Mixed Deep Reinforcement Learning Considering Discrete-continuous Hybrid Action Space for Smart Home Energy Management. *J. Mod. Power Syst. Clean Energy* **2022**, *10*, 743–754. [CrossRef]
37. Ale, L.; King, S.A.; Zhang, N. D3PG: Dirichlet DDPG for Task Partitioning and Offloading with Constrained Hybrid Action Space in Mobile Edge Computing. *IEEE Internet Things J.* **2021**, *9*, 19260–19272. [CrossRef]
38. Wu, J.; Wang, H.; Li, N. Formation Obstacle Avoidance: A Fluid-Based Solution. *IEEE Syst. J.* **2019**, *14*, 1479–1490. [CrossRef]
39. Xiong, J.; Wang, Q.; Yang, Z. Parametrized Deep Q-Networks Learning: Reinforcement Learning with Discrete-Continuous Hybrid Action Space. *arXiv* **2018**, arXiv:1810.06394. [CrossRef]

40. Schulman, J.; Wolski, F.; Dhariwal, P.; Radford, A.; Klimov, O. Proximal policy optimization algorithms. *arXiv* **2017**, arXiv:1707.06347. [CrossRef]
41. Wu, J.F.; Wang, H.L.; Wang, Y.X. UAV Reactive Interfered Fluid Path Planning. *Acta Autom. Sin.* **2021**, *47*, 1–16.